Diffusivity Reveals Three Distinct Phases of Interlayer Excitons in $MoSe_2/WSe_2$ Heterobilayers

Jue Wang,[1] Qianhui Shi,[2] En-Min Shih,[2] Lin Zhou,[1,3] Wenjing Wu,[1] Yusong Bai,[1] Daniel Rhodes,[4] Katayun Barmak,[5] James Hone,[4] Cory R. Dean,[2] and X.-Y. Zhu[1,*]

[1]*Department of Chemistry, Columbia University, New York, New York 10027, USA*
[2]*Department of Physics, Columbia University, New York, New York 10027, USA*
[3]*College of Engineering and Applied Sciences, Nanjing University, Nanjing 210093, People's Republic of China*
[4]*Department of Mechanical Engineering, Columbia University, New York, New York 10027, USA*
[5]*Department of Applied Physics and Applied Mathematics, Columbia University, New York, New York 10027, USA*

(Received 31 January 2020; revised 13 September 2020; accepted 25 January 2021; published 11 March 2021)

Charge separated interlayer excitons in transition metal dichalcogenide heterobilayers are being explored for moiré exciton lattices and exciton condensates. The presence of permanent dipole moments and the poorly screened Coulomb interaction make many-body interactions particularly strong for interlayer excitons. Here we reveal two distinct phase transitions for interlayer excitons in the $MoSe_2/WSe_2$ heterobilayer using time and spatially resolved photoluminescence imaging: from trapped excitons in the moiré potential to the modestly mobile exciton gas as exciton density increases to $n_{ex} \sim 10^{11}$ cm^{-2} and from the exciton gas to the highly mobile charge separated electron-hole plasma for $n_{ex} > 10^{12}$ cm^{-2}. The latter is the Mott transition and is confirmed in photoconductivity measurements. These findings set fundamental limits for achieving quantum states of interlayer excitons.

DOI: 10.1103/PhysRevLett.126.106804

In heterobilayers of semiconducting transition metal dichalcogenides (TMDCs), the type-II band alignment leads to the spatial separation of the electron-hole pair upon photoexcitation, forming long-lived interlayer excitons [1–5] that favor condensation [6–9]. The formation of moiré superlattices opens the door to a rich spectrum of phenomena from moiré exciton trapping [10,11] to topological mosaics [12] and correlated physics [13–15]. While the permanent dipoles promote many-body interactions for interlayer excitons, their properties also depend strongly on density. Recent experiments have suggested, at low densities, trapped excitons in moiré potentials [10,11,16–18] and, at high densities, a Mott transition between the exciton gas and a charge separated electron-hole plasma [3]. However, little is known about the transition from moiré trapped excitons to the free exciton gas and how properties vary across both phase transitions. Here we determine diffusivity of interlayer excitons in $MoSe_2/WSe_2$ heterobilayers over 4 orders of magnitude in excitation densities ($n_{ex} = 10^{9-14}$ cm^{-2}). We show that diffusivity increases by similar orders of magnitude with increasing n_{ex} across both phase transitions. The metallic nature of the charge separated electron-hole plasma is confirmed in photoconductivity.

We fabricate $MoSe_2/WSe_2$ heterobilayers using the transfer stacking technique from high-quality monolayers [19] and with hexagonal boron nitride (h-BN) encapsulation [20], as detailed elsewhere [3,11]. Interlayer exciton lifetimes as long as 200 ns and photogenerated n_{ex} as high as 10^{14} cm^{-2} have been demonstrated [3]. Optical microscope images of the three samples are shown in Fig. S1 of Supplemental Material (SM) [21]. All measurements are carried out at sample temperatures of 4 K and are completely reversible after repeated continuous wave (cw) or pulsed laser irradiation. In photoluminescence (PL) imaging measurements, we use two optically bright heterobilayers with small interlayer twist angles. We calibrate n_{ex} for the optically bright samples under both pulsed and cw conditions [3], Fig. S2 (SM [21]), and use the same calibration to estimate n_{ex} in the sample with no measurable PL (due to a large interlayer twist angle) used in photoconductivity measurement. The latter is a reasonable approximation as the dominant exciton species are the momentum indirect excitons with electrons in the Q valleys and holes in the K valleys [3,11,22]. The PL from minority bright excitons is in equilibrium with that from the majority dark excitons and lifetimes of the former reflect those of the latter, which are expected to be insensitive to twist angles.

To measure the diffusion coefficient (D), we photoexcite in a selected region and determine the spatial expansion of the interlayer excitons by scanning confocal PL microscopy [4,16,23,24]. We use the PL spectrum at ~1.35 eV from interlayer excitons or electron-hole plasmas [3,11] as a characteristic probe. We point out at the outset that all diffusion constants measured here represent apparent and averaged values on an inherently heterogeneous landscape for the interlayer excitons [11]. Figure 1(a) shows optical

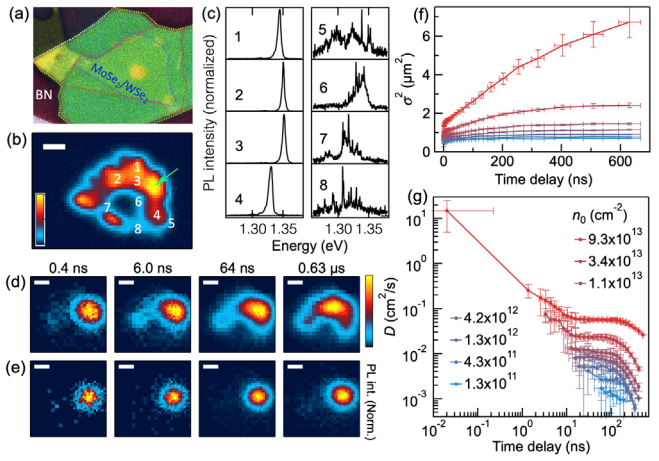

FIG. 1. Time-resolved diffusion in $MoSe_2/WSe_2$ heterobilayer. (a) Optical image of the h-BN encapsulated sample with interlayer twist angle $\Delta\theta = 2.6 \pm 0.5°$. The blue dashed outline shows the $MoSe_2/WSe_2$ heterobilayer region, with a bubble in the lower middle part. (b) Photoluminescence map from interlayer excitons in the $MoSe_2/WSe_2$ heterobilayer, showing the dark bubble. The green arrow points to the location of laser excitation in diffusion measurements. The numbers (1–8) in (b) mark the locations for PL spectra in (c). (d),(e) PL images at different t for high [$n_0 = 9.3 \times 10^{13}$ cm^{-2} (d)] and low [1.3×10^{12} cm^{-2} (e)] excitation densities. Scale bar, 2 μm. (f) Time-dependent spatial variance σ^2 and (g) effective diffusion coefficients as a function of time at different n_0. The first data point for $n_0 = 9.3 \times 10^{13}$ cm^{-2} was estimated from the initial spreading of the image beyond the laser excitation spot. Panels (a) and (c) are reproduced from Supplemental Material in Ref. [11]. Panels (b) and (c) were obtained with cw excitation at $h\nu = 2.33$ eV, $n_{ex} = 1.05 \times 10^{10}$ cm^{-2}. Panels (d)–(g) are from pulsed excitation (pulse width 100 fs) at $h\nu = 2.33$ eV. Sample temperature is 4 K.

image of one sample used in the imaging (Figs. 1 and 2). The blue dashed outline shows the region of the $MoSe_2/WSe_2$ heterobilayer. There is a bubble in the lower middle of the heterobilayer area with no PL, Fig. 1(b), while the surrounding area shows bright PL. Among the $MoSe_2/WSe_2$ heterobilayer samples fabricated [11], this sample shows a high level of spatial PL homogeneity [Fig. S3 (SM) [21]]. Spatially resolved PL from most spots in the bright region, Fig. 1(c) (left, from spots 1–4 in the PL image), are characteristic of PL from $MoSe_2/WSe_2$ heterobilayers in most reports to date [2–4].This so-called type-II PL was recently discovered to originate from one-dimensional (1D) strained moiré potentials [11]. The changes in peak position from spot to spot may be attributed to strain heterogeneity and there are also spots that show two or more peaks [11] [see Fig. 2(a)]. In regions with weak emission, near the edge of the heterobilayer region or the bubble, the PL spectra are as represented in Fig. 1(c) (right, from spots 5–8 in the PL image). This so-called type-I PL, with 10^{1-2} times lower intensity than those of type II, features sharp peaks that originate from unstrained zero-dimension (0D) moiré potentials traps [11]. In diffusion measurements based on total PL intensity, Figs. 1 and 2, contribution from type II dominates at earlier times and that from type I dominates at longer times ($\geq$100 ns; see below).

In time-resolved experiments, we photoexcite a diffraction-limited spot by an ultrafast laser pulse (width ~100 fs) and determine the PL intensity with temporal (~50 ps) and spatial (~0.2 μm) resolutions. Details on the experiments and analysis [25,26] can be found in SM [21]. Figures 1(d) and 1(e) show PL images at different time delays (t) for initial excitation densities of $n_0 = 9.3 \times 10^{13}$ cm^{-2} and $n_0 = 1.3 \times 10^{12}$ cm^{-2}, respectively. Diffusion is reflected in the spatial expansion of PL with t and it is faster at higher n_0. At $n_0 = 9.3 \times 10^{13}$ cm^{-2}, Fig. 1(d), the PL image fills the entire heterobilayer region for $t \geq 0.2$ μs. We fit the radial profile of the PL image at each t to a Gaussian function to obtain the spatial variance $\sigma^2(t)$, as detailed in Figs. S4–S7 (SM [21]). Figure 1(f) plots $\sigma^2(t)$ as functions of t, the slope of which gives the apparent diffusion coefficient, $D(t) = d\sigma^2(t)/dt$, Fig. 1(g).

While diffusivity generally decreases with time, Fig. 1(g), the shape of $D(t)$ reveals two distinct transitions: for $n_0 > n_{\mathrm{Mott}}$, $D(t)$ decreases initially until $t \sim 10^1$ ns, beyond which $D(t)$ becomes nearly a plateau; for $t > 10^2$ ns, $D(t)$ decreases again. At each n_0, the carrier density is substantially reduced during the initial rapid expansion from the diffraction-limited spot ($\sigma_0 \approx 0.3$ μm) within our time resolution. For $n_0 > n_{\mathrm{Mott}}$, this rapid expansion, attributed to ballistic transport and repulsive drift [27], leads to the Mott transition, the tail of which is captured in the drop of $D(t)$ for $t < 10^1$ ns. The second step occurs within the exciton phase and is characterized by a drastic decrease in $D(t)$ for $t > 10^2$ ns. The formation of the heterobilayer results in a moiré landscape consisting of quantum dot- or quantum wire-like local potential wells [28,29]. Trapping of interlayer excitons into the moiré potential wells [10,11] should drastically reduce diffusivity [16], as detailed below.

Complementary evidence can be found in cw PL imaging where the generation, recombination, and diffusion of the interlayer excitons reach a steady state. The excitation density at the center (n_c) reaches ~10^{14} cm^{-2} at the excitation spot and decays away from the center. The spatial distribution of n_{ex} allows probing of the phases [30] from the peak intensity (I_{PL}), width (full width at half maximum, FWHM), and average energy (E_{av}). Figure 2(a) shows normalized PL spectra at different n_c. The spectrum at $n_c \sim 10^{11}$ cm^{-2} mainly consists of one peak and, with increasing n_c, a peak on the high energy side grows in relative intensity. These two peaks presumably resulting from strain heterogeneity [11]. The peaks broaden with n_c, particularly across the Mott transition [3] and this is accompanied by blue shift in average peak energy, a result of dipolar repulsion. Figure S8 summarizes the overall or

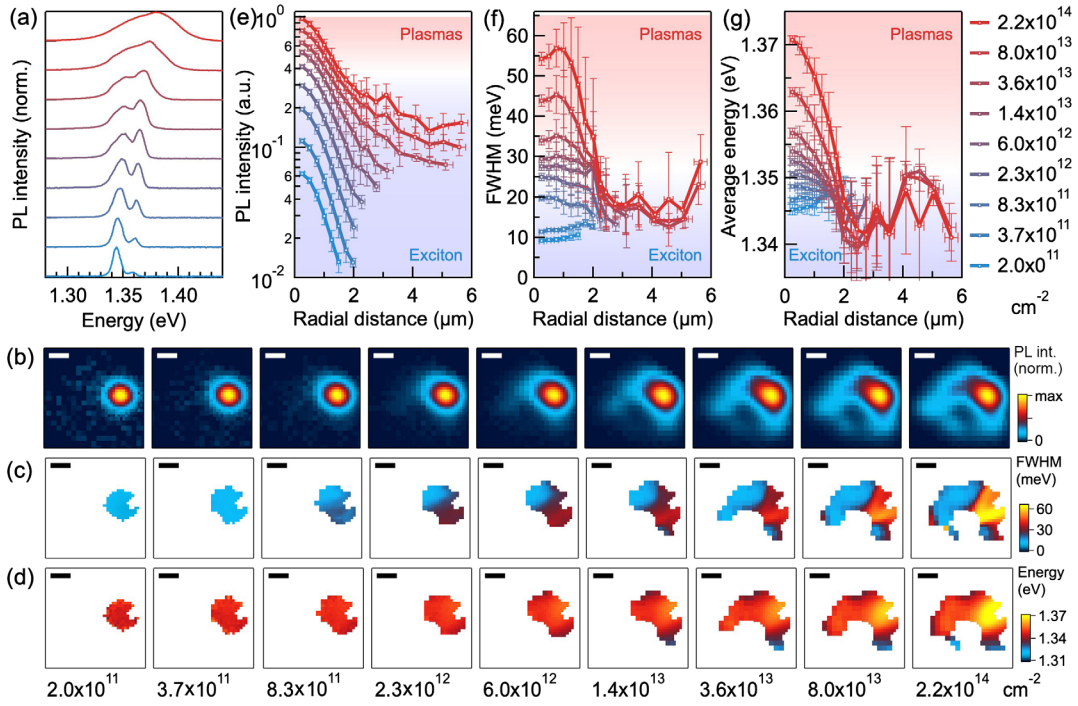

FIG. 2. Steady-state diffusion in the $MoSe_2/WSe_2$ heterobilayer. Interlayer twist angle $\Delta\theta = 2.6 \pm 0.5°$. The green arrow in Fig. 1(b) marks the center of the excitation spot in this cw imaging experiment. (a) PL spectra at the center excitation spot as a function of excitation density (bottom to top: 2.0×10^{11}–2.2×10^{14} cm^{-2}). Each spectrum is normalized at the peak intensity and offset vertically for clarity). (b)–(d) Image of PL intensity, FWHM, and average energy at different excitation densities, from 2.0×10^{11} cm^{-2} (leftmost) to 2.2×10^{14} cm^{-2} (rightmost), as listed in the legend below (d). Scale bar, 2 μm. (e)–(g) PL intensity, FWHM, and average energy as a function of radial distance from excitation spot at different excitation densities. The plasmas phase is within ~2 μm of the excitation spot at high n_{ex}. cw excitation at $h\nu = 2.33$ eV.

individual FWHM, and average peak energy, E_{av} as a function of n_{ex} (SM [21]).

We show spatial maps of I_{PL} [Fig. 2(b)], FWHM [Fig. 2(c)], and E_{av} [Fig. 2(d)] for $n_c = 2.0 \times 10^{11}$ – 2.2×10^{14} cm^{-2}. A detailed analysis can be found in SM, Figs. S9 and S10 [21]. For $n_c < n_{\mathrm{Mott}}$, both FWHM and E_{av} are spatially uniform, consistent with a single phase of interlayer exciton gas. For $n_c > n_{\mathrm{Mott}}$, both FWHM and E_{av} clearly show spatial gradients that correspond to the central plasma phase and the exciton gas phase away from the center. We show the three quantities as a function of radial distance (ρ) from the center; see Figs. 2(e)–2(g). The plots of FWHM and E_{av} reveal a phase boundary at $\rho \sim 2$ μm, within which the system is in the plasma phase at $n_c > n_{\mathrm{Mott}}$. For $\rho > 2$ μm, the system is in the exciton gas phase, independent of n_c. From a diffusion length of ~2 μm and lifetime of $\tau \sim 20$ ns, we estimate $D = l^2/\tau \sim 2$ cm^2/s, which is close to the average for $D \sim 15$–0.2 cm^2/s for the plasma in time-resolved imaging experiments. At the high cw excitation densities for the plasma phase, the potential presence of thermal gradient may contribute to the fast diffusion within $\rho \sim 2$ μm.

To focus on the transition from moiré exciton trapping to exciton gas, we switch to a $MoSe_2/WSe_2$ sample which features only quantum emitter-like type-I PL (Fig. S11 [21]). Figure 3(a) shows n_c-dependent PL spectra from a typical spot. At $n_{ex} \leq 10^{11}$ cm^{-2}, the multiple sharp PL peaks are indicative of 0D moiré excitons [10,11,17]. For $n_{ex} = \sim 5 \times 10^{11}$ cm^{-2}, the sharp PL peaks merge into one or two broadened peaks, suggesting that the interlayer excitons move out of the 0D moiré traps to form a free exciton gas. Further broadening is seen for $n_{ex} > 10^{12}$ cm^{-2}, as expected for the Mott transition. Figure 3(b) plots calculated moiré supercell densities as a function of twist angle ($\Delta\theta$) for $MoSe_2/WSe_2$ (blue), and other TMDC heterobilayers. The $\Delta\theta = 1.6°$ corresponds to a moiré supercell density of $n_{\mathrm{moiré}} = 8 \times 10^{11}$ cm^{-2}. The experimental trap-to-gas transition density of $\sim 1-5 \times 10^{11}$ cm^{-2} is below $n_{\mathrm{moiré}}$. Dipolar and exchange repulsion makes it improbable to occupy every moiré trap.

We show in Fig. 3(c) the I_{PL} images for $n_c = 8 \times 10^9$ – 5×10^{11} cm^{-2}; type-I PL emission dominates in this low-density range. At the lowest n_c, the Gaussian width σ is ~0.5 μm [Fig. 4(b)], close to the theoretical diffraction limit of $\sigma* = 0.21\lambda/\mathrm{NA} = 0.3$ μm [31]. We estimate upper and lower bounds of D by taking the initial size of the excitation spot as either σ^* or the lowest experimental value ($\sigma \sim 0.5$ μm). Figure 3(e) shows the estimated D as a function of n_c; each data point is an average from these two limits. The diffusion constants are in the range of

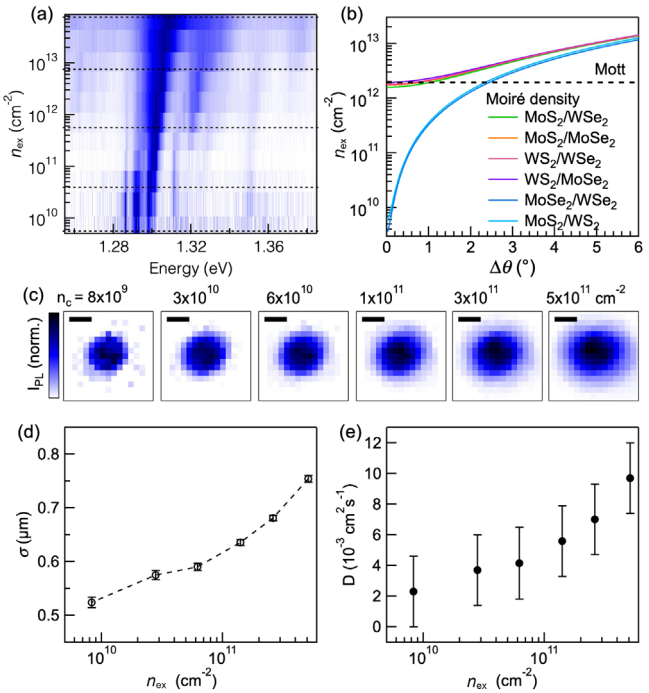

FIG. 3. Moiré exciton trapping in the $MoSe_2/WSe_2$ heterobilayer. Interlayer twist angle $\Delta\theta = 1.6 \pm 0.4°$. (a) Pseudocolor (normalized intensity) of PL spectra as a function of excitation density. (b) Calculated moiré supercell density as a function of interlayer twist angle for $MoSe_2/WSe_2$ (blue) and five other TMDC heterobilayers. (c) cw PL images at different center excitation densities from 8×10^9 cm^{-2} to 5×10^{11} cm^{-2}. Scale bar, 1 μm. (d) Gaussian width at different center densities. (e) Apparent diffusion constants estimated from the Gaussian width in (d).

10^{-3} cm^2/s, similar to the lower limit in time-resolved experiments at $n_{ex} \sim 10^{11}$ cm^{-2} [Fig. 1(g)]. The increasing D with n_c is also confirmed in spatial correlation analysis (Fig. S12 [21]).

The apparent diffusivity for moiré trapped interlayer excitons is surprising, as the depths of moiré exciton traps of $U = 20$–100 meV [28,29] make thermally activated hopping negligible at 4 K. U can be overcome by a high T or n_{ex} and modeled as $D = D_0 \exp(-(U/kT + u_0 n_{ex}))$ [16]. Yuan *et al.* reported an interexciton repulsion energy, due mainly to exchange interaction, of $u_0 \sim 1.6 \times 10^{-14}$ eV/cm^2 for interlayer excitons in the WS_2/WSe_2 heterobilayer [16]. If we use the same value, overcoming the $U = 20$–100 meV moiré potential trap to give measurable diffusion would require a high electronic temperature $T > 200$–$1200\ K$ at the low n_{ex} limit or an $n_{ex} > 1.2 \times 10^{12}$–$6.2 \times 10^{12}$ cm^{-2} at 4 K. For cold excitons at the densities we use in Fig. 3, both T and n_{ex} are over 2 orders of magnitude lower than those required for measurable diffusion. The observed residual diffusion may come from nonequilibrium interlayer excitons before they are completely cooled down and localized to the moiré traps, as there is ~300 meV excess energy when interlayer excitons form from intralayer excitons [1–3,22].

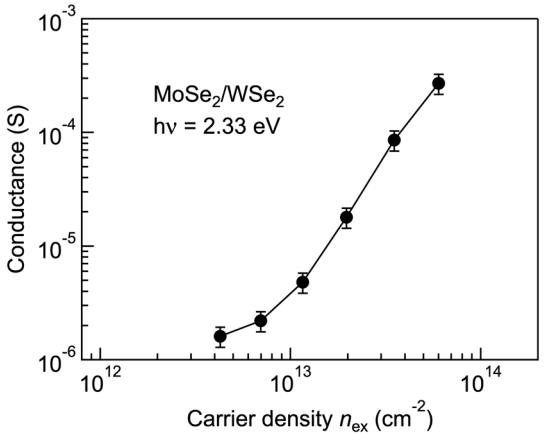

FIG. 4. Photoconductance of $MoSe_2/WSe_2$ heterobilayer. Interlayer twist angle $\Delta\theta > 5°$. Conductivity as a function of photoexcited density at $h\nu = 2.33$ eV showing an insulator state to metal transition. The onset of photoconductivity is close to the Mott density, $n_{\mathrm{Mott}} \sim 1.6$–$3 \times 10^{12}$ cm^{-2}.

We now return to the Mott transition, the most direct confirmation of which comes from the conductive nature of the plasma. Figure 4 shows photoconductivity as a function of n_{ex} at zero gate voltage in a four-terminal device (Figs. S13 and S14 [21]) under cw excitation ($h\nu = 2.33$ eV). Conductivity is not measurable at $n_{ex} \leq n_{\mathrm{Mott}}$, as expected from the insulating exciton gas. Above n_{Mott}, photoconductivity rises rapidly by more than 2 orders of magnitude as n_{ex} increases from 4×10^{12} cm^{-2} to 6×10^{13} cm^{-2}. This provides direct evidence for the insulator-to-metal transition [32], the threshold of which is in agreement with the spectroscopically or theoretically determined $n_{\mathrm{Mott}} \sim 1.6$–$3 \times 10^{12}$ cm^{-2} [3].

Our results quantitatively establish two phase transitions in the $MoSe_2/WSe_2$ heterobilayer: from the moiré trapped excitons to the free interlayer exciton gas and further to the conducting electron-hole plasmas. Interlayer excitons in TMDC heterobilayers are thought to be excellent model systems for exciton condensation [6,7]. Our results indicate that the free interlayer exciton picture, widely assumed in the literature, only exists in the narrow density range around 10^{11}–10^{12} cm^{-2}. In the low-density range, our results also reveal limits for achieving a localized moiré exciton lattice [28] due to dipolar repulsion. At the high n_{ex} limit, the charge separated nature of the degenerate electron-hole plasmas means that the sheet of electrons or holes in each TMDC monolayer is similar to those from gate-doped TMDCs, where superconductivity at 2D carrier densities in the 10^{14} cm^{-2} range has been reported [33–36]. This raises the tantalizing possibility of achieving cw photoinduced superconductivity in TMDC heterobilayers, provided cooling of the plasmas can be realized for sufficiently long-lived charge separation.

We thank Hanqing Xiong for help with scanning confocal microscopy and Kenji Watanabe and Takashi Taniguchi for providing *h*-BN crystals. All spectroscopy experiments were supported by the National Science Foundation (NSF) Grant No. DMR-1809680. Photoconductivity measurements were supported by the Materials Science and Engineering Research Center (MRSEC) through NSF Grant No. DMR-1420634 and 2011738.

*xyzhu@columbia.edu

[1] X. Hong, J. Kim, S. F. Shi, Y. Zhang, C. Jin, Y. Sun, S. Tongay, J. Wu, Y. Zhang, and F. Wang, Nat. Nanotechnol. **9**, 682 (2014).
[2] P. Rivera, J. R. Schaibley, A. M. Jones, J. S. Ross, S. Wu, G. Aivazian, P. Klement, K. Seyler, G. Clark, N. J. Ghimire, J. Yan, D. G. Mandrus, W. Yao, and X. Xu, Nat. Commun. **6**, 6242 (2015).
[3] J. Wang, J. Ardelean, Y. Bai, A. Steinhoff, M. Florian, F. Jahnke, X. Xu, M. Kira, J. Hone, and X.-Y. Zhu, Sci. Adv. **5**, eaax0145 (2019).
[4] L. A. Jauregui, A. Y. Joe, K. Pistunova, D. S. Wild, A. A. High, Y. Zhou, G. Scuri, K. De Greve, A. Sushko, C.-H. Yu, T. Taniguchi, K. Watanabe, D. J. Needleman, M. D. Lukin, H. Park, and P. Kim, Science **366**, 870 (2019).
[5] P. Merkl, F. Mooshammer, P. Steinleitner, A. Girnghuber, K. Q. Lin, P. Nagler, J. Holler, C. Schüller, J. M. Lupton, T. Korn, S. Ovesen, S. Brem, E. Malic, and R. Huber, Nat. Mater. **18**, 691 (2019).
[6] F.-C. Wu, F. Xue, and A. H. MacDonald, Phys. Rev. B **92**, 165121 (2015).
[7] M. M. Fogler, L. V. Butov, and K. S. Novoselov, Nat. Commun. **5**, 4555 (2014).
[8] O. L. Berman and R. Y. Kezerashvili, Phys. Rev. B **93**, 245410 (2016).
[9] Z. Wang, D. A. Rhodes, K. Watanabe, T. Taniguchi, J. C. Hone, J. Shan, and K. F. Mak, Nature (London) **574**, 76 (2019).
[10] K. L. Seyler, P. Rivera, H. Yu, N. P. Wilson, E. L. Ray, D. G. Mandrus, J. Yan, W. Yao, and X. Xu, Nature (London) **567**, 66 (2019).
[11] Y. Bai, L. Zhou, J. Wang, W. Wu, L. McGilly, D. Halbertal, C. F. B. Lo, F. Liu, J. Ardelean, P. Rivera, N. R. Finney, X. Yang, D. N. Basov, W. Yao, X. Xu, J. Hone, A. Pasupathy, and X.-Y. Zhu, Nat. Mater. **19**, 1068 (2020).
[12] Q. Tong, H. Yu, Q. Zhu, Y. Wang, X. Xu, and W. Yao, Nat. Phys. **13**, 356 (2017).
[13] Y. Tang, L. Li, T. Li, Y. Xu, S. Liu, K. Barmak, K. Watanabe, T. Taniguchi, A. H. MacDonald, J. Shan, and K. F. Mak, Nature (London) **579**, 353 (2020).
[14] E. C. Regan, D. Wang, C. Jin, M. I. Bakti Utama, B. Gao, X. Wei, S. Zhao, W. Zhao, Z. Zhang, K. Yumigeta, M. Blei, J. D. Carlström, K. Watanabe, T. Taniguchi, S. Tongay, M. Crommie, A. Zettl, and F. Wang, Nature (London) **579**, 359 (2020).
[15] Y. Shimazaki, I. Schwartz, K. Watanabe, T. Taniguchi, M. Kroner, and A. Imamoğlu, Nature (London) **580**, 472 (2020).
[16] L. Yuan, B. Zheng, J. Kunstmann, T. Brumme, A. B. Kuc, C. Ma, S. Deng, D. Blach, A. Pan, and L. Huang, Nat. Mater. **19**, 617 (2020).
[17] W. Li, X. Lu, S. Dubey, L. Devenica, and A. Srivastava, Nat. Mater. **19**, 624 (2020).
[18] J. Choi, W.-T. Hsu, L.-S. Lu, L. Sun, H.-Y. Cheng, M.-H. Lee, J. Quan, K. Tran, C.-Y. Wang, and M. Staab, Sci. Adv. **6**, eaba8866 (2020).
[19] D. Edelberg, D. Rhodes, A. Kerelsky, B. Kim, J. Wang, A. Zangiabadi, C. Kim, A. Abhinandan, J. Ardelean, M. Scully, D. Scullion, L. Embon, R. Zu, E. J. G. Santos, L. Balicas, C. Marianetti, K. Barmak, X. Zhu, J. Hone, and A. N. Pasupathy, Nano Lett. **19**, 4371 (2019).
[20] O. Ajayi, J. Ardelean, G. Shepard, J. Wang, A. Antony, T. Taniguchi, K. Watanabe, T. Heinz, S. Strauf, and X. Y. Zhu, 2D Mater. **4**, 031011 (2017).
[21] See Supplemental Material at http://link.aps.org/supplemental/10.1103/PhysRevLett.126.106804 for materials and methods, additional data and analysis.
[22] R. Gillen and J. Maultzsch, Phys. Rev. B **97**, 165306 (2018).
[23] P. Rivera, K. L. Seyler, H. Yu, J. R. Schaibley, J. Yan, D. G. Mandrus, W. Yao, and X. Xu, Science **351**, 688 (2016).
[24] D. Unuchek, A. Ciarrocchi, A. Avsar, Z. Sun, K. Watanabe, T. Taniguchi, and A. Kis, Nat. Nanotechnol. **14**, 1104 (2019).
[25] N. S. Ginsberg and W. A. Tisdale, Annu. Rev. Phys. Chem. **71**, 1 (2020).
[26] T. Zhu, J. M. Snaider, L. Yuan, and L. Huang, Annu. Rev. Phys. Chem. **70**, 219 (2019).
[27] Z. Vörös, R. Balili, D. W. Snoke, L. Pfeiffer, and K. West, Phys. Rev. Lett. **94**, 226401 (2005).
[28] W. Yao, X. Xu, G.-B. Liu, J. Tang, and H. Yu, Sci. Adv. **3**, e1701696 (2017).
[29] K. Tran *et al.*, Nature (London) **567**, 71 (2019).
[30] M. Stern, V. Garmider, E. Segre, M. Rappaport, V. Umansky, Y. Levinson, and I. Bar-Joseph, Phys. Rev. Lett. **101**, 257402 (2008).
[31] B. Zhang, J. Zerubia, and J. C. Olivo-Marin, Appl. Opt. **46**, 1819 (2007).
[32] V. M. Asnin and A. A. Rogachev, JETP Lett. **7**, 360 (1968).
[33] L. J. Li, E. C. T. O'Farrell, K. P. Loh, G. Eda, B. Ozyilmaz, and A. H. C. Neto, Nature (London) **529**, 185 (2016).
[34] Y. Saito, Y. Nakamura, M. S. Bahramy, Y. Kohama, J. Ye, Y. Kasahara, Y. Nakagawa, M. Onga, M. Tokunaga, T. Nojima, Y. Yanase, and Y. Iwasa, Nat. Phys. **12**, 144 (2016).
[35] J. M. Lu, O. Zheliuk, I. Leermakers, N. F. Q. Yuan, U. Zeitler, K. T. Law, and J. T. Ye, Science **350**, 1353 (2015).
[36] J. M. Lu, O. Zheliuk, Q. H. Chen, I. Leermakers, N. E. Hussey, U. Zeitler, and J. T. Ye, Proc. Natl. Acad. Sci. U.S.A. **115**, 3551 (2018).